Dalton Transactions

ROYAL SOCIETY OF CHEMISTRY

PAPER

View Article Online
View Journal | View Issue

Cite this: *Dalton Trans.*, 2026, **55**, 3310

Galvanic-displacement-derived CuO_x–Pt/Cu interfaces for *operando* activation and enhanced HER in acidic media

Pracheta Trivedi,[a] Sandeep Yadav,[a] Neha Clare Minj,[a] Balakumaran Kamaraj,[a] Sneha Mittal,[a] Shivani Saraswat,[a] Subramanian Natarajan[b,c] and Anantharaj Sengeni *[a]

This work presents an interesting and easy galvanic displacement strategy for the synthesis of self-supported Pt–Cu heterointerfaces optimized for the hydrogen evolution reaction (HER) in acidic media. By galvanically replacing surface copper with Pt^{2+} ions, we achieve a unique CuO_x–Pt/Cu interface, which undergoes dynamic *in situ* activation during the HER to form a Pt–Cu_2O/Cu heterostructure, in which Pt is present in trace amounts. This transformation significantly enhanced the electrocatalytic HER requiring just 38 mV and 76 mV as overpotentials for 10 and 100 mA cm^{-2}, respectively, outperforming bulk Pt foil. The synergistic interplay between Pt, Cu_2O, and Cu is believed to have delivered superior charge transfer and active-site stabilization, while the self-supporting architecture improves catalyst durability and accessibility. Our approach demonstrates scalable, cost-efficient catalyst fabrication that maximizes Pt utilization while minimizing Pt consumption, providing a promising pathway toward next-generation HER electrocatalysts for efficient green hydrogen production under acidic conditions with ultralow Pt content.

Received 11th December 2025,
Accepted 19th January 2026

DOI: 10.1039/d5dt02961a

rsc.li/dalton

Introduction

The global transition toward a sustainable and carbon-neutral energy infrastructure has ignited intense research into hydrogen production through water electrolysis.[1] Among various electrochemical processes, the hydrogen evolution reaction (HER) in acidic media remains central to industrial-scale hydrogen generation due to its favorable kinetics and compatibility with proton exchange membrane (PEM) electrolyzers.[2–4] However, the widespread deployment of PEM-based hydrogen technologies is constrained by the reliance on platinum-group metals (PGMs), particularly Pt, which stands as the most active and stable HER catalyst in acidic environments.[5] Although Pt exhibits near-thermodynamic activity for the Volmer–Tafel/Heyrovsky steps, its scarcity and escalating cost demand innovative strategies that drastically reduce Pt loading without compromising catalytic performance or long-term operational durability.[6] Substantial progress has been made in lowering the Pt content of catalysts through alloying, nanostructuring, and heterointerfacing with other cheap and abundant metals.[7–15] Such approaches also aim to tune the hydrogen-binding energy (HBE), modulate the local density of states, and accelerate interfacial charge transfer. Nevertheless, most strategies continue to require usage of high amounts of Pt or involve multistep synthetic procedures that lack scalability and produce catalysts that are only effective under low current densities (<200 mA cm^{-2}), which are far below industrially practical values.[16] Cu-based substrates, especially Cu foams and Cu mesh, can be attractive platforms for designing low-Pt HER catalysts. Cu is Earth-abundant, highly conductive, easily machinable, and compatible with diverse transformation chemistries.[17] Importantly, Cu readily undergoes surface oxidation (forming Cu_2O/CuO) and can act as a redox-active scaffold whose electronic structure can be dynamically tuned under electrochemical operation.[18,19] Recent studies have shown that constructing Pt–Cu interfaces can substantially enhance HER activity due to favorable charge redistribution, synergistic hydrogen adsorption–desorption energetics and facilitated water dissociation steps.[7,8,20,21] A notable study on this is that recently reported by Wang and co-workers who made Pt/CuO nanoclusters on a porous MOF-derived N-doped carbon support for the HER.[22] Furthermore, Kaya and co-workers showed that catalysts with Pt–Cu nanoparticle interfaces provide less energy-demanding reaction pathways for the HER than those of both Pt and Cu.[23] Very recently, Guo and

[a]*Laboratory for Electrocatalysis and Energy, Department of Chemistry, Indian Institute of Technology, Kanpur 208 016, Uttar Pradesh, India. E-mail: ananths@iitk.ac.in*
[b]*Electroplating & Electrometallurgy Division (EPEMD), CSIR-Central Electrochemical Research Institute (CECRI), Karaikdui-630003, Tamil Nadu, India*
[c]*Academy of Scientific and Innovative Research (AcSIR), Ghaziabad-201 002, India*

co-workers showed the design and application of ultralow Pt-containing CuO_x for total water splitting and methyl orange photodegradation,[24] while Anand and coworkers fabricated 3D mesostructured electrodes with a Cu/CuO_x microstructure using a 3D printing method to enhance the electron transport and facilitate the removal of gas bubbles from the electrode.[13,25] In addition to this, there have been many studies that employed CuPt alloys as HER electrocatalysts and electrochemical sensing platforms reported in the literature.[26–29] Yet, most of these Pt–Cu heterostructures were produced through high-temperature or chemical-intense routes that restrict interfacial intimacy and stability. Galvanic displacement, in contrast, offers a simple, room-temperature, and highly surface-selective approach to deposit trace amounts of Pt onto metallic Cu.[20,30–32] By exploiting the difference in standard reduction potentials between Pt^{2+}/Pt (+1.18 V *vs.* reversible hydrogen electrode (RHE)) and Cu^{2+}/Cu (+0.34 V *vs.* RHE), Pt^{2+} ions can spontaneously replace surface Cu atoms without the need for external reducing agents. This method not only guarantees strong anchoring of Pt species but also generates a mixed oxide/hydroxide environment around Cu that can evolve dynamically during the HER process. Such spontaneous surface reconstruction pathways are rarely leveraged in HER catalyst design for acidic media, albeit they are quite well known for alkaline media.

In this work, we report a galvanic-displacement-assisted fabrication of CuO_x–Pt/Cu (initial state) that undergoes *operando* activation during the HER to form a highly active and stable Pt–Cu_2O/Cu heterostructured self-supported electrode. The as-prepared electrode, referred to as CuO_x–Pt/Cu, was produced by immersing metallic Cu in a dilute Pt^{2+} solution, where Cu atoms were partially replaced to generate atomically dispersed Pt/PtO species intimately integrated with CuO/Cu. Upon cathodic polarization in acidic electrolyte, this mixed-valence heterostructure underwent a series of HER potential-driven transformations such as the reduction of PtO to metallic Pt and the partial reduction of CuO to Cu_2O. Unlike conventional electrochemical preconditioning, no specific pre-electrolysis was needed to facilitate this transformation and concurrent activation. It occurred spontaneously at the first application of HER potentials. Hence, we call it *operando* activation rather than electrochemical conditioning. Due to these concurrent surface chemical transformations, an electrically percolated Pt–Cu_2O–Cu interface emerged. This *operando*-formed Pt–Cu_2O constitutes the true catalytically active state and is responsible for the exceptional HER performance. Such *in situ* activation pathways are increasingly recognized as vital for understanding and optimizing real-world electrocatalysts.

Experimental

Materials and fabrication of Pt–PtO–CuO/Cu

To fabricate the structurally dynamic CuO_x–Pt/Cu system, Cu foam strips procured from Nanoshel® were first surface-cleaned in 3 M HCl to remove passive oxides. The cleaned Cu foam strips (1 cm × 3 cm) were then immersed in a 10 mmol solution of $PtCl_2$ (Sigma Aldrich®) and stirred for 3 h at room temperature. This process facilitated the formation of isolated Pt nanoparticles on the surface-oxidized Cu foam. At the end of the reaction, the Cu foam strips turned dark grey, indicating the formation of CuO. The corresponding reaction occurring under these conditions is presented in eqn (1):

$$Cu^0 + Pt^{2+} \rightarrow Cu^{2+} + Pt^0 \quad (1)$$

The above reaction is driven by the highly positive reduction potential of the Pt^{2+}/Pt couple (+1.18 V *vs.* RHE). It was observed that extending the stirring time beyond 3 h led to the formation of a thick CuO layer that detached easily upon exposure to the electrolyte. Conversely, a reaction time shorter than 2 h resulted in insufficient surface coverage of Pt nanoparticles on the Cu foam, limiting the enhancement in HER activity. After the reaction, the Cu foam strips were collected, spray-washed with deionized water to remove loosely bound ions and dried at room temperature. The dried electrode was directly used for *operando* activation and subsequent physicochemical characterization. Both the as-prepared and *operando*-activated electrodes were comparatively examined to comprehensively understand the structural transformations occurring during *operando* activation.

Electrochemical characterizations

All electrochemical measurements were performed in 0.5 M H_2SO_4 using a Hg/Hg_2SO_4 reference electrode and an anodized Ti foil as the counter electrode. The potential of the reference electrode and the pH were calibrated by measuring the onset potential of the HER with a Pt foil electrode. Cyclic voltammograms (CVs) were recorded at a scan rate of 50 mV s^{-1} without applying *iR* compensation. In contrast, linear sweep voltammograms (LSVs) were acquired at a slower scan rate of 5 mV s^{-1} with *iR* correction to evaluate the intrinsic catalytic activity and extract the Tafel slope (but not the exchange current density). All the current densities obtained in LSV and CV measurements were normalized with the geometric area of the working electrode to evaluate the respective current densities. Although this might not enable direct comparison because the differences in surface roughness and actual surface area could lead to misleading assessments of catalytic activity, this is the best way to show the explicit differences in their apparent activities. Electrochemical impedance spectroscopy (EIS) was conducted over a potential range spanning the non-catalytic to catalytic turnover regions to assess changes in intrinsic conductivity and charge-transfer characteristics induced during the activation process. The electrode stability under a constant applied potential was evaluated by chronoamperometry (CA) at −0.26 V *vs.* RHE. Unless stated otherwise, all potentials were converted to the RHE scale. All precautionary measures, including reference electrode calibration, pH measurement, and *iR* drop compensations, were taken according to the guidelines available through various electrochemical tutorials in the literature.[33–37]

Results and discussion

Operando activation and electrocatalytic HER studies

The prepared CuO_x–Pt/Cu electrode, obtained *via* galvanic displacement of Cu by Pt^{2+}, was initially electrochemically cycled in 0.5 M H_2SO_4 at a scan rate of 50 mV s^{-1} within the potential range of 0.195 V to −0.645 V *vs.* RHE (Fig. 1a). During the first cycle, a pronounced reduction peak appeared between 0.195 V and −0.485 V *vs.* RHE, corresponding to the reduction processes $Cu^{2+} \rightarrow Cu$, $Cu^{2+} \rightarrow Cu^{+}$, and $Pt^{2+} \rightarrow Pt$.[38–42] These reduction processes likely occurred simultaneously, as indicated by the immediate color transition of the electrode surface from dark grey to a characteristic Cu_2O and metallic Cu hue. Notably, no blue coloration of the electrolyte was observed, confirming the absence of Cu^{2+} dissolution despite the strong acidic (pH 0) environment. These observations col-

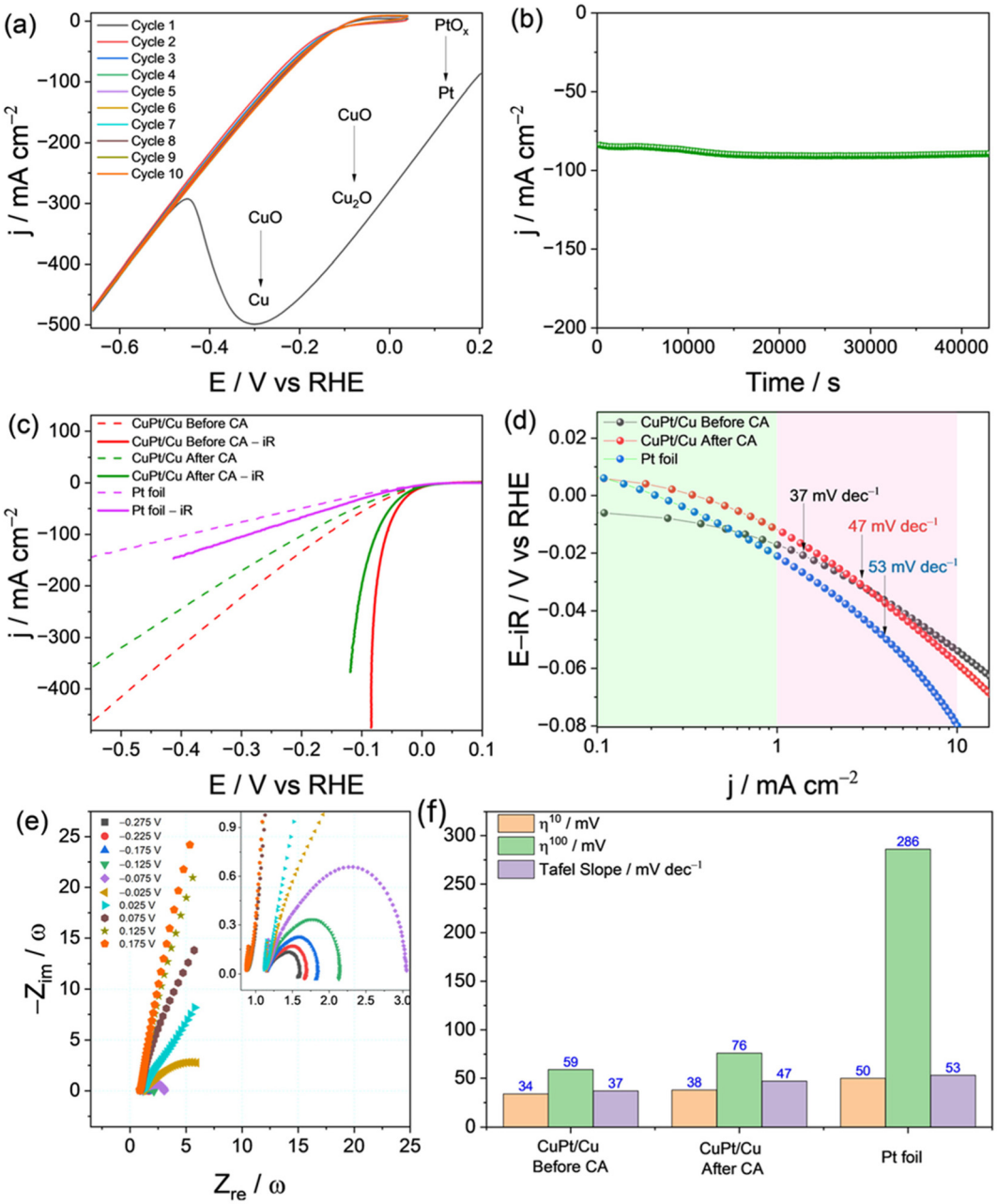

Fig. 1 (a) The first 10 CV cycles of CuO_x–Pt/Cu performed in 0.5 M H_2SO_4 at a scan rate of 50 mV s^{-1}, showing *in situ* activation behavior. (b) HER chronoamperometric (CA) analysis of the *in situ* activated electrode conducted at −0.26 V *vs.* RHE, demonstrating the long-term stability of the catalyst under acidic HER conditions. (c) HER LSVs of the same activated electrode conducted with and without *iR* drop correction compared to that of the Pt foil. (d) Corresponding Tafel plots. (e) Multi-potential EIS analysis-derived Nyquist plots, illustrating charge transfer kinetics of the catalyst during the HER. (f) Benchmarking metrics of the same catalyst before and after CA, compared with the metrics of the Pt foil.

lectively suggest that the intense reduction peak in the first cycle mainly arises from the reduction of Cu^{2+} (formed *via* galvanic oxidation of Cu by Pt^{2+}) to Cu^{+} and metallic Cu species on the electrode surface. As the anodic potential was increased beyond 0.195 V, significant oxidation and dissolution of Cu were evident from the noticeable change in the electrolyte's color, thereby obscuring any detectable Pt^{2+}/Pt redox features. Nonetheless, any residual Pt^{2+} species on the surface were likely reduced to Pt, given the sufficiently cathodic potentials applied.

At the cathodic vertex potential of −0.645 V *vs.* RHE, a large HER current density of approximately −475 mA cm^{-2} was recorded during the first cycle and was sustained over the subsequent nine cycles without noticeable attenuation. The persistence of this high HER current indicates that *operando* activation of the as-prepared electrode occurred rapidly within the first cycle, rendering additional activation treatments unnecessary. Thus, the electrode can undergo self-activation under applied cathodic potentials during the initial HER screening itself. With this *operando*-activated electrode, an endurance test at −0.26 V *vs.* RHE was performed to determine whether the initial electrochemical activation was sufficient or if the electrode still possessed room for further dynamic changes that could influence its HER behavior in acid. The CA response shown in Fig. 1b exhibited a smooth and stable *j*–*t* profile, indicating that no notable surface reconstruction occurred during extended operation that could affect the HER activity. This observation reinforces that a single application of a cathodic potential (or even a single cathodic sweep) is sufficient to activate the electrode and generate a high-performance, highly stable HER catalyst. To obtain a comparative and comprehensive assessment of its performance, the HER activity of the CuO_x–Pt/Cu electrode was evaluated before and after CA and compared with that of a Pt foil electrode (Fig. 1c). Both *iR*-corrected and as-acquired LSVs clearly demonstrated that the CuO_x–Pt/Cu electrode produced *via* simple galvanic displacement and subsequently activated during HER operation, outperformed the state-of-the-art Pt foil in the acidic HER, particularly under proton-rich conditions. However, it should be noted that while this common practice provides a useful baseline, it does not account for differences in surface roughness or real surface area, factors that significantly influence geometric current density and thus limit a rigorous assessment of intrinsic activity. After CA, a slight decrease in HER activity was observed without any shift in the onset potential, suggesting that the minor activity loss is extrinsic in nature and the intrinsic activity remains intact. Notably, even after this small decline, the CuO_x–Pt/Cu electrode still delivered better performance than Pt foil under identical experimental conditions. The fully *iR*-corrected (100%) LSVs were then used to construct the corresponding Tafel plots (Fig. 1d). Though this is not an ideal method, it does provide a very close estimate of the real Tafel slopes. The calculated Tafel slopes for CuO_x–Pt/Cu before and after CA were 37 and 47 mV dec^{-1}, respectively, indicating a marginal change in HER kinetics following the endurance test. Consistent with the overpotential trends, the Tafel slopes of CuO_x–Pt/Cu (both before and after CA) remained lower than that of Pt foil, confirming faster hydrogen evolution kinetics on the CuO_x–Pt/Cu surface.

To understand how *operando* activation influenced the charge-transfer characteristics, a series of EIS measurements were performed at potentials ranging from 0.175 V to −0.275 V *vs.* RHE, and the corresponding Nyquist plots are shown in Fig. 1e. As evident from these plots, shifting the applied potential to being increasingly cathodic (from −0.025 V *vs.* RHE onward) resulted in a progressive decrease in the charge-transfer resistance (R_{ct}), consistent with the accelerated HER kinetics at more negative potentials. In the potential window between 0.175 and 0.025 V *vs.* RHE (in the cathodic direction), the charge-transfer behavior was not purely resistive but exhibited a significant capacitive contribution, as reflected by the Warburg-like feature inclined toward the *y*-axis. This indicates that the reactions occurring prior to the HER onset were governed by a combination of charge-transfer and mass-transport processes. The only plausible reactions in this potential domain that exhibit such dual control are the reduction of Cu^{2+} to Cu^{+} or Cu, and the reduction of Pt^{2+} to Pt. Hydrogen underpotential deposition (HUPD) could also contribute; however, given the extremely low Pt content on the electrode surface, the likelihood of extensive HUPD is minimal. Therefore, we attribute the observed capacitive behavior primarily to the reduction of metal ions during the early stages of activation. Interestingly, the uncompensated resistance (R_u) increased by approximately 0.4 Ω when the applied potential approached the HER onset. This likely arises from the formation of Cu_2O on the electrode surface, which can slightly decrease the electronic conductivity of metallic Cu. Taken together, the EIS results clearly support the occurrence of *operando* activation in the CuO_x–Pt/Cu electrode as it progresses toward HER-relevant potentials, as reflected by the evolving charge-transfer characteristics. To present a direct comparison of the HER metrics before and after CA, the overpotentials at −10 and −100 mA cm^{-2} and the corresponding Tafel slopes are summarized in Fig. 1f. The combined *operando* activation and HER electrocatalytic analyses strongly demonstrate that the fabricated CuO_x–Pt/Cu electrode, despite containing ultra-low amounts of Pt, has the potential to replace bulk Pt or Pt/C electrodes in commercial electrolyzer applications.

Probing the changes brought about by *operando* activation

Diffractometric and spectroscopic studies. To evaluate how *operando* activation altered the surface solid-state characteristics of the CuO_x–Pt/Cu electrode, X-ray diffraction (XRD) patterns were recorded before and after CA and compared with that of bare Cu foam (Fig. 2a). The bare Cu foam (black) showed the expected metallic Cu diffraction peaks (denoted by #), along with only very weak signals corresponding to surface oxides.[43–45]

In contrast, the CuO_x–Pt/Cu electrode before CA (red) exhibited reflections attributable to both CuO (denoted by $) and Cu_2O (denoted by *), indicating that the galvanic-displacement process produced a mixture of CuO and Cu_2O.[17,46–49]

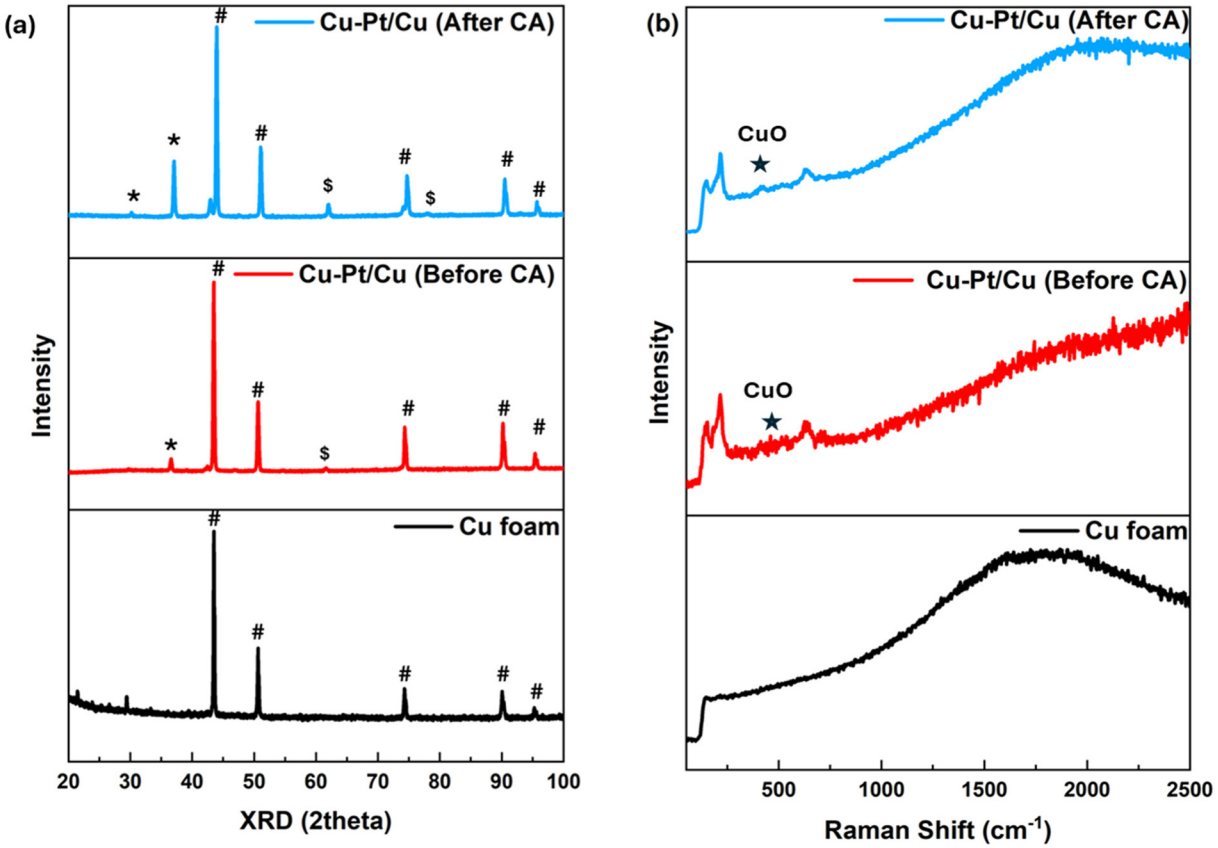

Fig. 2 XRD patterns (a) and Raman spectra (b) of the Cu foam substrate, CuO_x–Pt/Cu before CA, and CuO_x–Pt/Cu after CA. These were recorded to determine how the galvanic-displacement reaction and the *operando* activation facilitated surface chemistry changes.

After CA, the CuO_x–Pt/Cu electrode (blue) displayed markedly intensified Cu_2O peaks, confirming that CuO was predominantly reduced to Cu_2O during *operando* activation. The metallic Cu reflections were also strengthened following CA, suggesting concurrent reduction of CuO to metallic Cu. Correspondingly, the CuO peak intensities diminished substantially, supporting the *in situ* conversion of CuO to Cu_2O and Cu. The observed diffraction peaks of Cu, Cu_2O, and CuO matched JCPDS card numbers 00-001-1242, 00-034-1354, and 01-078-0428, respectively. Notably, no X-ray diffracting Pt nanoparticles were detected from the patterns. Raman spectroscopy (Fig. 2b) was further employed to probe the surface chemical features of bare Cu, CuO_x–Pt/Cu before CA, and CuO_x–Pt/Cu after CA.[17,19] As expected, the cleaned Cu foam did not display Cu oxide or hydroxide Raman modes, as incident photons were largely reflected due to the metallic and lustrous surface. In contrast, both CuO_x–Pt/Cu samples exhibited characteristic Cu–O stretching and bending vibrational bands within the 700–200 cm^{-1} region, consistent with the presence of surface copper oxides.

However, Raman spectroscopy cannot discriminate between Cu_2O and CuO, necessitating the use of more definitive surface-sensitive techniques such as X-ray photoelectron spectroscopy (XPS). Comprehensive XPS analyses were therefore performed on CuO_x–Pt/Cu before CA (Fig. 3a–d) and after CA (Fig. 4a–d), and the corresponding narrow scans for C 1s, O 1s, Cu 2p, and Pt 4f were examined. The C 1s spectra of both samples (Fig. 3a and 4a) displayed a strong C–sp^3 signal, which was used for charge calibration of the O, Cu, and Pt regions. Subsequently, the O 1s spectra of CuO_x–Pt/Cu before and after CA (Fig. 3b and 4b) were analyzed. Before CA, the surface was predominantly covered by M–O species between 529.5 and 531.8 eV, within which two peaks could be deconvoluted. The lower-intensity peak at 529.5 eV corresponds to Cu_2O, while the higher-binding-energy component is attributed to CuO.[19] A noticeable contribution from $Cu(OH)_2$ was also observed near 531.9 eV. It is also plausible that a fraction of the M–O signal originates from PtO formed by precipitation and dehydration.[21] After CA, the intensities of peaks associated with M–O and M–OH species decreased by more than 50%, indicating a substantial reduction in surface oxide and hydroxide content.

However, these features were not eliminated entirely, suggesting that the reductive environment during CA was insufficient to induce complete reduction. The Cu 2p spectra of CuO_x–Pt/Cu before and after CA (Fig. 3c and 4c) conveyed similar information, with the same features present in both cases but with reduced intensities after CA. Since in the Cu 2p

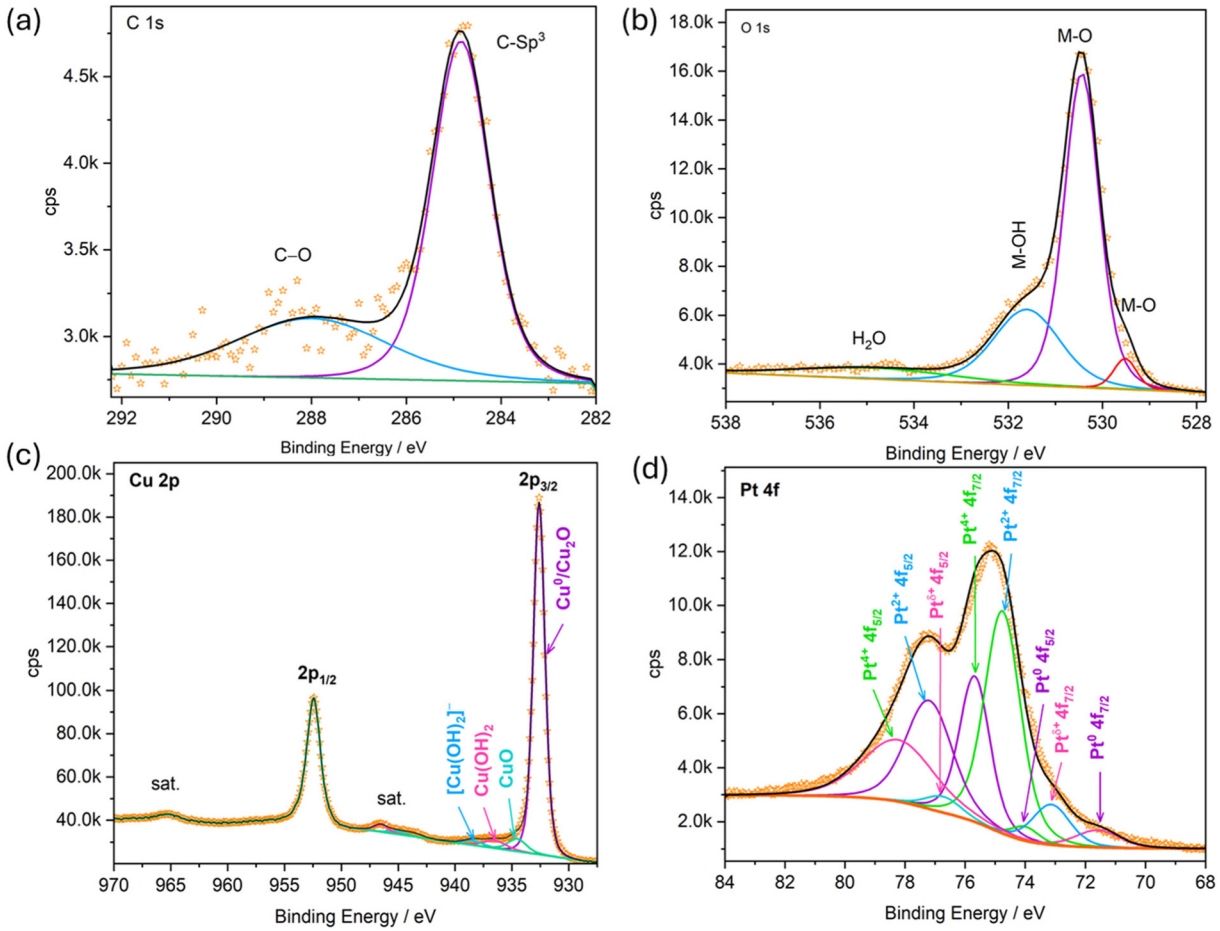

Fig. 3 (a–d) XPS narrow scans of C 1s, O 1s, Cu 2p, and Pt 4f of CuO_x–Pt/Cu before CA, respectively. All the narrow scans were calibrated by taking the C 1s as the reference.

XPS signals for Cu^0 and Cu^+ cannot be distinguished, the peak at ~931 eV is attributable to both oxidation states. As Cu_2O, and in fact all copper species, exhibit negligible HER electrocatalytic activity, further differentiation at this stage is unnecessary. The most revealing insights from the XPS analysis were obtained from the Pt 4f spectra (Fig. 3d and 4d).

Before CA, the Pt 4f region showed a dominant Pt^{2+} signal along with measurable contributions from Pt^0 and $Pt^{\delta+}$ species (intermediate valence states between 0 and +2). This confirms that galvanic displacement occurred, but that a substantial fraction of Pt remained unreduced on the surface. The precise amount of metallic Pt cannot be quantified by XPS. However, we hypothesize that the Pt^0 generated initially by reduction of Pt^{2+} by Cu^0 was buried beneath the surface, while the subsequently formed CuO/Cu_2O matrix trapped a significant proportion of unreduced Pt^{2+}. This scenario is beneficial, as exposure to HER-relevant reductive potentials would convert trapped Pt^{2+} to Pt^0 *in situ*, generating additional HER-active sites. If this hypothesis were correct, the Pt 4f spectrum obtained after CA should exhibit a dominant Pt^0 signal. As anticipated, the post-CA spectrum revealed intense and sharp peaks at 71.5 eV ($4f_{7/2}$) and 73.9 eV ($4f_{5/2}$) corresponding to Pt^0, along with enhanced $Pt^{\delta+}$ contributions. This confirms that a substantial fraction of Pt^{2+} present in the as-prepared CuO_x–Pt/Cu surface was reductively converted to Pt^0 during *operando* activation. Despite this strong evidence from XPS, no Pt reflections were detected in the XRD patterns, implying that the resulting Pt crystallites were too small to produce observable diffraction signals.

Microscopic and macroscopy-associated spectroscopic studies. The surface morphological features of CuO_x–Pt/Cu were first examined using scanning electron microscopy (SEM). Fig. 5a–c shows the SEM images of bare Cu foam, which exhibit the expected smooth metallic surface. In contrast, the surface of CuO_x–Pt/Cu before CA (Fig. 5d–f) displayed a markedly roughened texture with large, well-defined crystals exhibiting clear faceting. As evident in Fig. 5f, many of these crystals terminate with the (111) plane, characteristic of CuO. In addition to these large crystallites, numerous highly contrasted Pt nanoparticles (NPs) were observed on the cracked and textured underlayer, indicating successful galvanic displacement that produced both CuO crystallites and Pt NPs on the surface prior to CA. Following CA, the same CuO_x–Pt/Cu electrode was re-examined by SEM, and the resulting images are

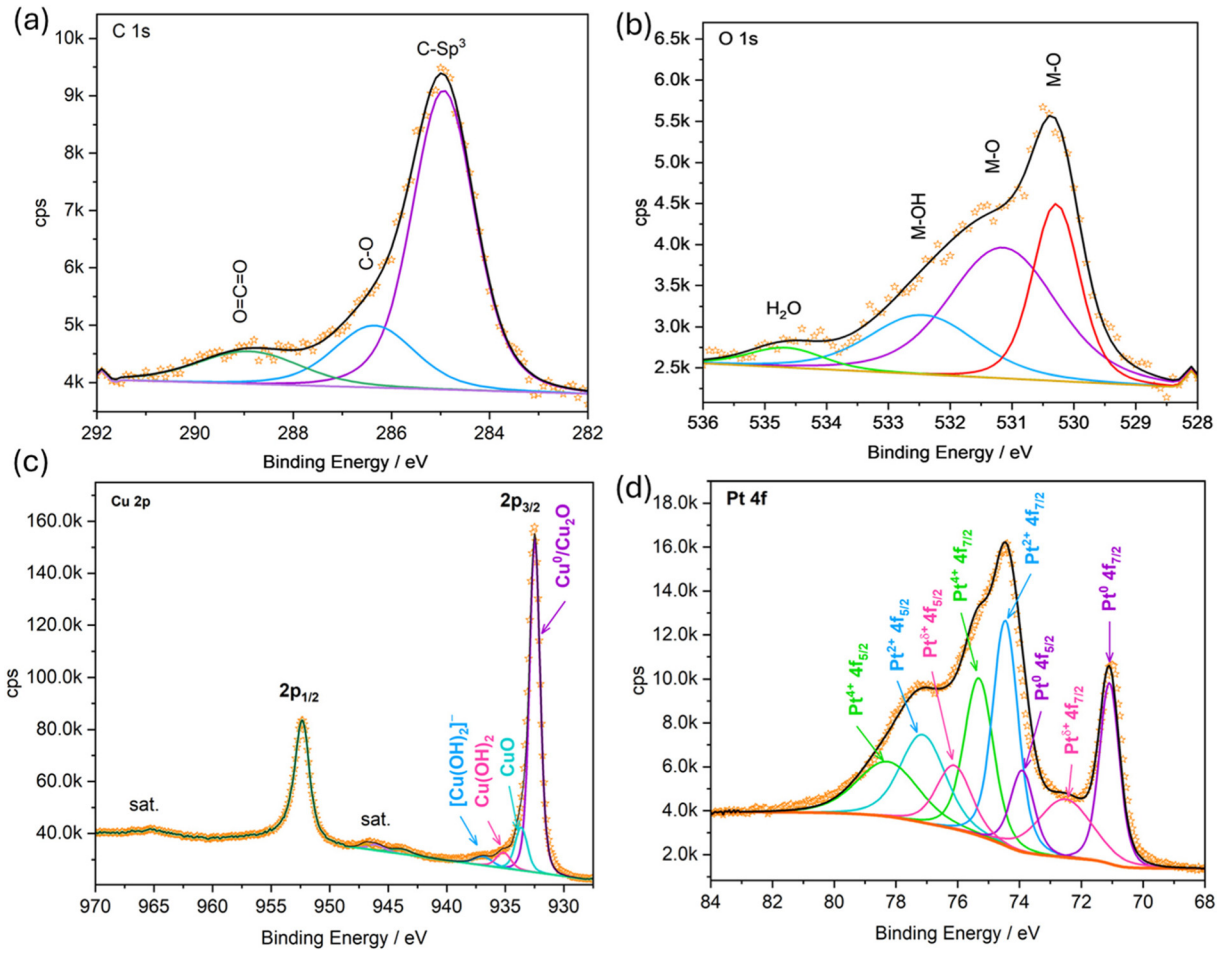

Fig. 4 (a–d) XPS narrow scans of C 1s, O 1s, Cu 2p, and Pt 4f of CuO_x–Pt/Cu after CA, respectively. All the narrow scans were calibrated by taking the C 1s as the reference.

shown in Fig. 5g–i. The surface roughness increased substantially, suggesting extensive surface reconstruction, consistent with expectations from *operando* activation. The CuO crystals observed before CA were no longer present, indicating their significant reduction during CA. Concurrently, it was noted that the highly contrasted Pt NPs increased in size, implying further *in situ* electrochemical reduction of residual Pt^{2+} during the HER.

These enlarged Pt NPs arising from *operando* reduction are clearly visible in Fig. 5h and i. Collectively, the SEM observations corroborate the structural and chemical transformations inferred from XRD and XPS analyses. Energy-dispersive X-ray spectroscopy (EDS) measurements for all three samples (Fig. S1a–c) showed that the bare Cu foam was free of oxygen and impurities, whereas the Pt content in CuO_x–Pt/Cu decreased from 2.69 atomic% before CA to 0.15 atomic% after CA. Although this trend contrasts with the XPS-derived interpretation, the reduction in Pt content may be partially attributed to CuO leaching during CA, which could remove surface-bound Pt nanoparticles along with the dissolved copper species.

To further examine the morphology and solid-state characteristics of the surface constituents of CuO_x–Pt/Cu before and after CA, the electrodes were gently ultrasonicated to detach the surface layer and disperse it in water. The resulting homogenized suspensions were drop-cast onto carbon-coated Cu grids for transmission electron microscopy (TEM). Fig. 6a–c shows TEM images of the material removed from the CuO_x–Pt/Cu surface before CA. Consistent with the SEM observations, the previously observed crystalline domains appear ruptured and transformed into randomly oriented sheet-like fragments.

The high-resolution image (Fig. 6c) reveals highly monodisperse Pt nanoparticles (NPs) embedded within these sheets, which are likely composed of copper oxides and hydroxides. The measured *d*-spacings correspond to metallic Pt, confirming that galvanic displacement successfully reduced Pt^{2+} to Pt^0 using Cu as the reducing substrate. The Pt NPs exhibited an average diameter of 4.11 nm (Fig. S2a and b).

Achieving such monodispersity without structure-directing agents, surfactants, or ligands underscores the effectiveness of the synthesis method. TEM images of the material removed from CuO_x–Pt/Cu after CA (Fig. 6d–f) again reveal entangled

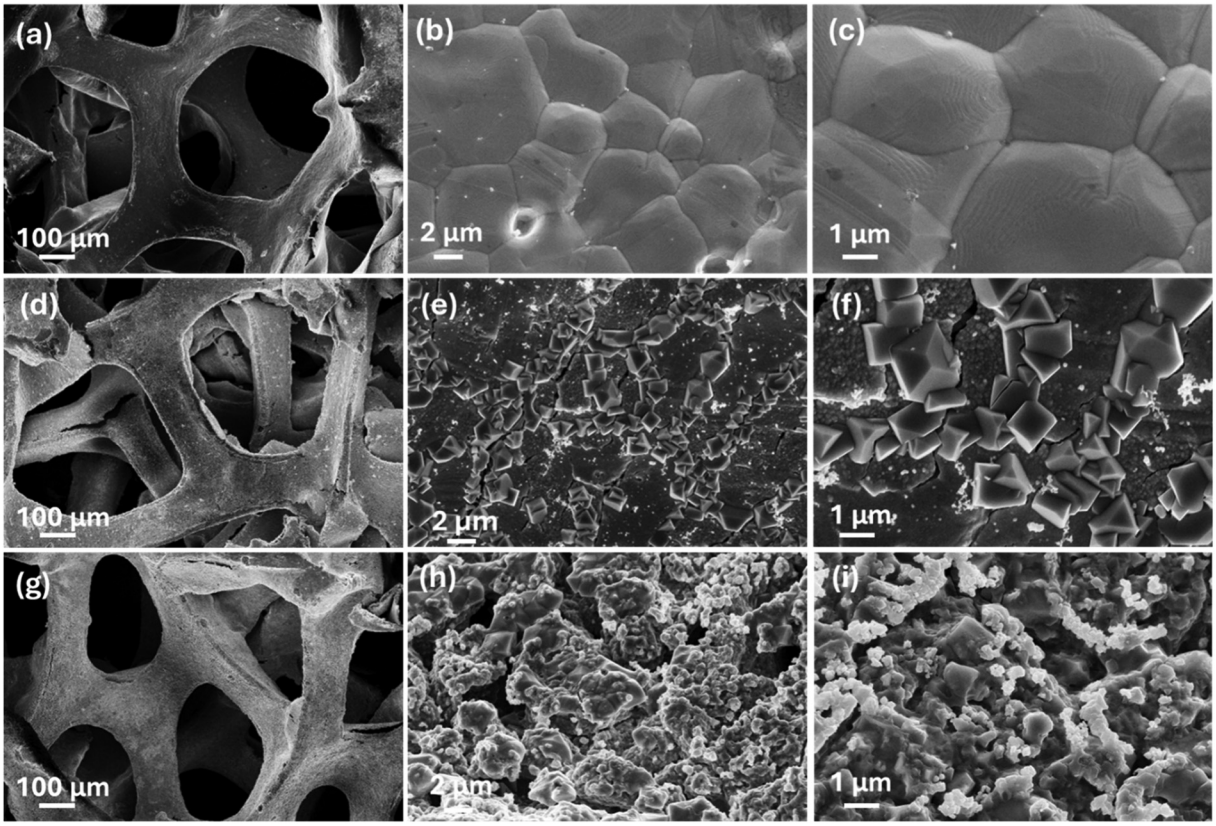

Fig. 5 SEM images of Cu foam (a–c), CuO_x–Pt/Cu before CA (d–f), and CuO_x–Pt/Cu after CA (g–i). All these images show clear changes in morphologies and surface topography as the displacement reaction and *operando* activation progressed.

sheets derived from copper oxide layers. At higher resolution, larger crystallites with *d*-spacings primarily corresponding to Cu_2O were observed, aligning with the color change noted during *operando* activation. The circled crystallites correspond to Pt NPs, which retained their average size. This explains the absence of Pt reflections in the XRD analysis: the nanoparticles are too small to generate detectable diffraction patterns yet are clearly visible in the TEM images. To assess the compositional uniformity of Cu and Pt in the segregated surface material before and after CA, elemental mapping was performed in scanning TEM (STEM) mode (Fig. 7a and b). The STEM images and corresponding Cu and Pt maps show that both elements are uniformly distributed across the examined domains. The associated EDS spectra (Fig. S3a and b) confirm the absence of impurity elements. To determine whether Cu and Pt existed as discrete domains rather than as a homogeneous alloy (CuPt), EDS line scans were collected from individual particles before and after CA (Fig. 8a and b).

The complementary nature of the Pt (green) and Cu (red) signals indicates that Pt and Cu occupy distinct regions, confirming a heterostructured material rather than an alloy. Notably, this heterostructure was retained even after 12 h under strongly reductive HER conditions, indicating that *operando* activation selectively generated isolated Pt NPs rather than CuPt alloy nanoparticles. The STEM EDS analysis also reveals that Pt is more uniformly dispersed prior to CA and becomes less uniformly distributed after CA, suggesting that surface Pt species may have been redistributed or dynamically reorganised under sustained cathodic potential, where Pt likely coalesces into larger, richer domains *via* mechanisms such as Ostwald ripening or agglomeration.[50–52] This redistribution and growth process is a common feature of nanoparticle activation under operational conditions and is often associated with the stabilization of catalytic activity. Selected area electron diffraction (SAED) was also performed on the segregated material before and after CA (Fig. S4a–d). For CuO_x–Pt/Cu before CA (Fig. S4a and b), SAED patterns collected from Pt nanoparticles displayed distinct diffraction spots corresponding to the (111) and (311) planes of Pt. In contrast, patterns collected from the encapsulating sheets exhibited ring and spot features characteristic of CuO and Cu_2O. After CA (Fig. S4c and d), the number and intensity of Cu_2O ring and spot patterns increased significantly, indicating extensive conversion of CuO to Cu_2O, consistent with the observed color change from dark grey to orange-red. Overall, the combined diffraction, microscopy, and spectroscopy analyses demonstrate that Pt^{2+} displaced Cu^0 from the Cu foam substrate and deposited onto its oxidized surface primarily as Pt nanoparticles, with a fraction of Pt^{2+} remaining trapped within the copper oxide matrix. During the HER, this trapped Pt^{2+} was

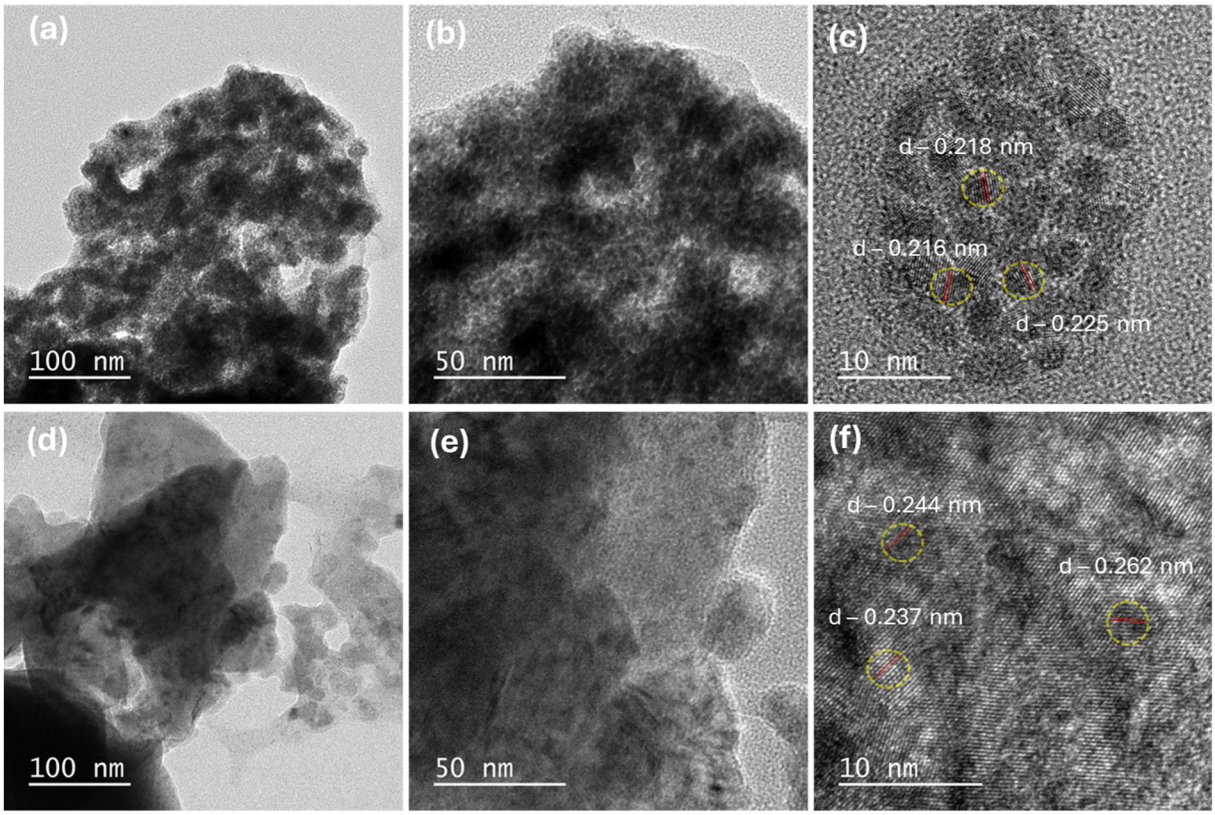

Fig. 6 TEM images of the surface constituents of CuO_x–Pt/Cu electrode before (a–c) and after (d–f) CA.

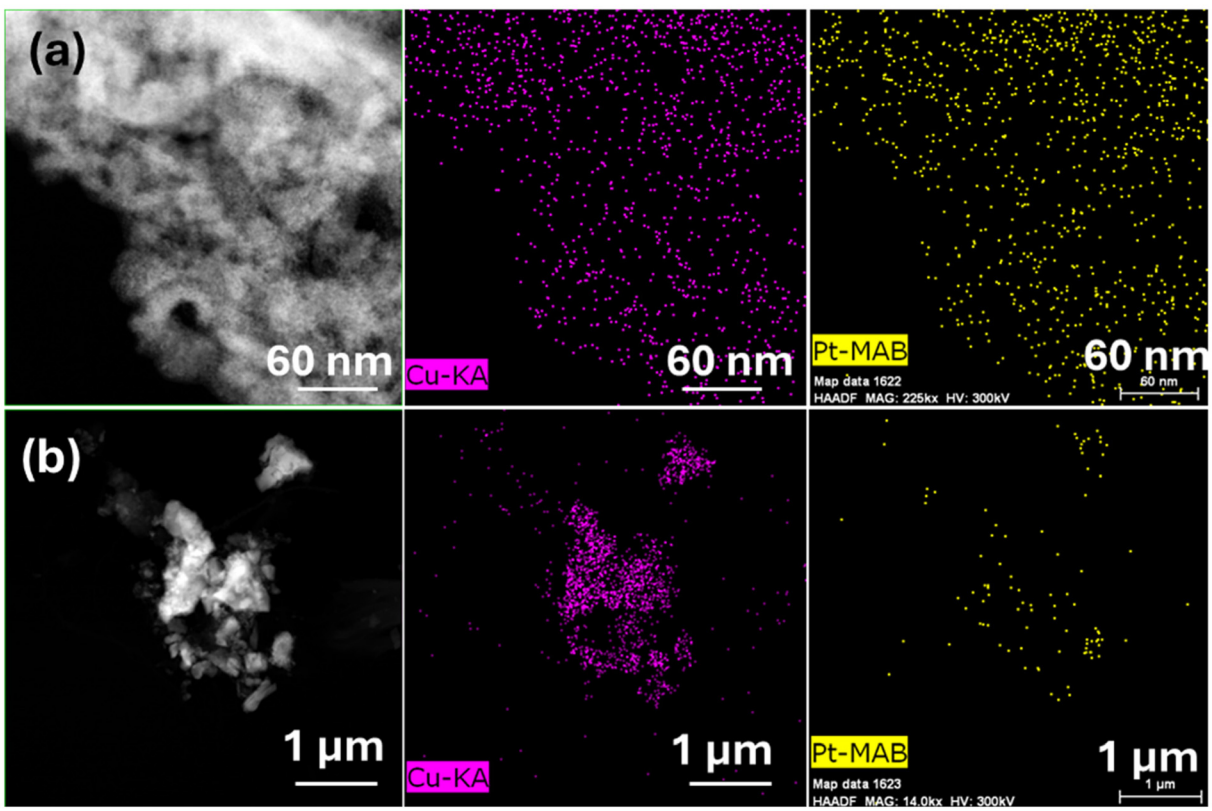

Fig. 7 STEM-HAADF images of surface constituents of CuO_x–Pt/Cu before (a) and after (b) CA with their corresponding Cu (pink) and Pt (yellow) EDS elemental maps.

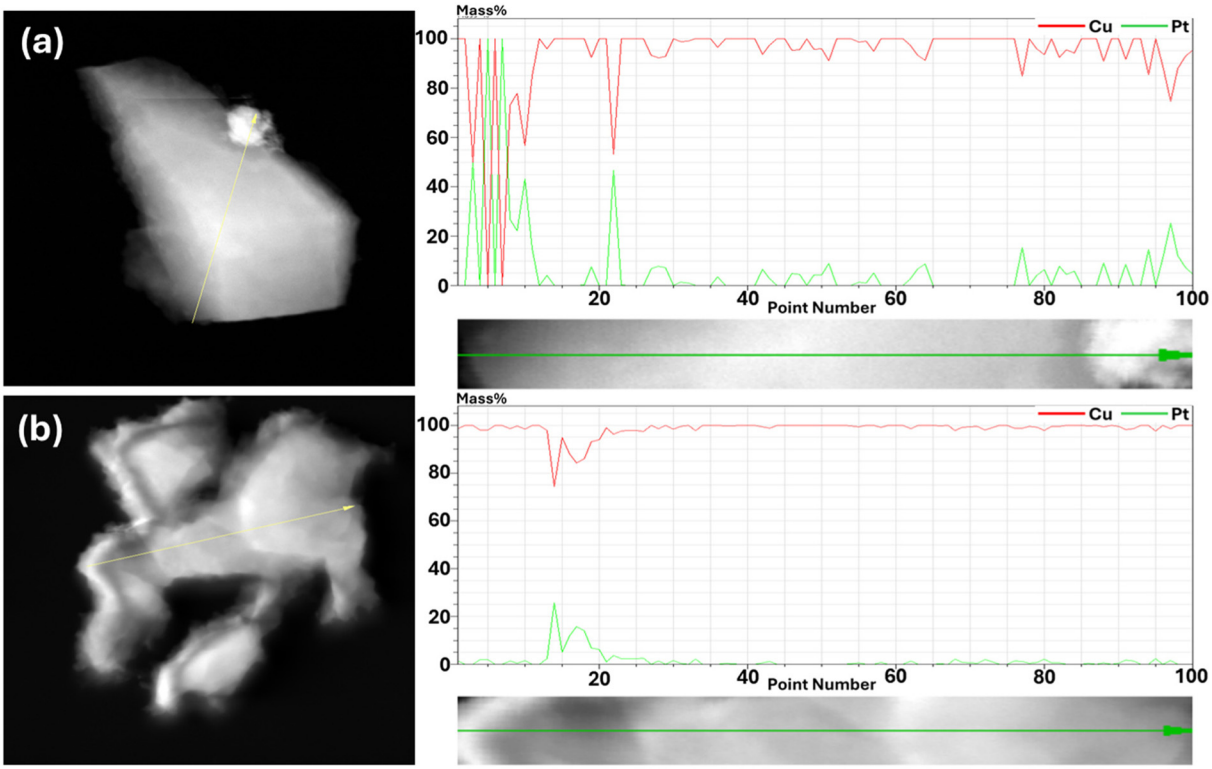

Fig. 8 STEM-HAADF images of the surface constituents of CuO_x–Pt/Cu before (a) and after (b) CA and their corresponding EDS elemental line maps, in which red indicates Cu and green indicates Pt.

reduced *in situ* to Pt^0, leading to *operando* activation of the CuO_x–Pt/Cu self-supported electrode, which enabled its HER performance to surpass that of the Pt foil in acidic media.

Conclusions

In summary, this study establishes a simple yet powerful galvanic-displacement strategy for constructing self-supported Cu–Pt heterostructured electrodes with ultralow Pt loading for the efficient hydrogen evolution reaction (HER) in acidic media. By replacing surface Cu^0 with Pt^{2+}, a CuO_x–Pt/Cu interface was initially generated, in which a significant fraction of Pt remained trapped in oxidized Cu domains. Comprehensive structural, spectroscopic, and microscopic investigations confirmed the coexistence of metallic Pt nanoparticles and copper oxide phases, with Pt predominantly present as ~4 nm monodisperse NPs embedded within CuO/Cu_2O nanosheets. During the HER, this surface underwent *operando* reconstruction, wherein trapped Pt^{2+} was reduced *in situ* and CuO was largely converted to Cu_2O, yielding an activated Pt–Cu_2O/Cu interface. This dynamic transformation enhanced charge transfer, stabilized active sites, and increased accessible catalytic regions, leading to remarkable electrocatalytic performance with overpotentials of only 38 mV and 76 mV at 10 and 100 mA cm^{-2}, respectively, surpassing the performance of bulk Pt foil despite the trace Pt content. The self-supported configuration eliminated polymeric binders, improved mass transport, and contributed to long-term stability over extended operation. Importantly, the catalyst design maximizes Pt utilization efficiency while conserving precious-metal usage, offering a scalable and cost-effective route toward high-performance acidic HER electrodes. Collectively, this work opens a promising avenue for next-generation HER electrocatalysts that couple ultralow Pt usage with superior activity, stability, and manufacturability for green hydrogen production.

Author contributions

P. T.: conceptualization, methodology, validation, formal analysis, investigation, data curation, writing – original draft, and visualization. S. Y., N. C. M., B. K., S. M., and S. S.: investigation, data curation, writing – original draft, and visualization. N. S.: validation, formal analysis, investigation, data curation, writing – original draft, and visualization. A. S.: conceptualization, methodology, validation, formal analysis, investigation, resources, data curation, writing – original draft, writing – review & editing, visualization, supervision, project administration, and funding acquisition.

Conflicts of interest

The authors declare no competing interests.

Data availability

All the data discussed in this work are provided in full in the main manuscript and the supplementary information (SI). Supplementary information: SEM-ED spectra, TEM-ED spectra and SAED patterns. See DOI: https://doi.org/10.1039/d5dt02961a.

Access to unprocessed data will be given upon a reasonable request made *via* an email addressed to the corresponding author.

Acknowledgements

This work was supported by the PMECR grant from ANRF, India (ANRF/ECRG/2024/000063/CS). CSIR-CECRI Manuscript number: CECRI/PESVC/Pubs/2025- 172.

References

1 M. Chatenet, B. G. Pollet, D. R. Dekel, F. Dionigi, J. Deseure, P. Millet, R. D. Braatz, M. Z. Bazant, M. Eikerling, I. Staffell, P. Balcombe, Y. Shao-Horn and H. Schäfer, Water Electrolysis: From Textbook Knowledge to the Latest Scientific Strategies and Industrial Developments, *Chem. Soc. Rev.*, 2022, **51**(11), 4583–4762, DOI: 10.1039/D0CS01079K.

2 Y. Cheng and S. P. Jiang, Advances in Electrocatalysts for Oxygen Evolution Reaction of Water Electrolysis-from Metal Oxides to Carbon Nanotubes, *Prog. Nat. Sci.:Mater. Int.*, 2015, **25**(6), 545–553, DOI: 10.1016/j.pnsc.2015.11.008.

3 W. Li, H. Tian, L. Ma, Y. Wang, X. Liu and X. Gao, Low-Temperature Water Electrolysis: Fundamentals, Progress, and New Strategies, *Mater. Adv.*, 2022, **3**(14), 5598–5644, DOI: 10.1039/D2MA00185C.

4 K. Ayers, High Efficiency PEM Water Electrolysis: Enabled by Advanced Catalysts, Membranes, and Processes, *Curr. Opin. Chem. Eng.*, 2021, **33**, 100719, DOI: 10.1016/j.coche.2021.100719.

5 J.-W. Zhao, K. Yue, H. Zhang, S.-Y. Wei, J. Zhu, D. Wang, J. Chen, V. Y. Fominski and G.-R. Li, The Formation of Unsaturated IrOx in SrIrO3 by Cobalt-Doping for Acidic Oxygen Evolution Reaction, *Nat. Commun.*, 2024, **15**(1), 2928, DOI: 10.1038/s41467-024-46801-y.

6 S. Anantharaj, Hydrogen Evolution Reaction on Pt and Ru in Alkali with Volmer-Step Promotors and Electronic Structure Modulators, *Curr. Opin. Electrochem.*, 2022, **33**, 100961, DOI: 10.1016/j.coelec.2022.100961.

7 S. T. Döşlü and A. Döner, Electrochemical Behavior of Pt Nano-Particles Dispersed on Cu/Ni Electrode in Alkaline Environment, *Int. J. Hydrogen Energy*, 2024, **75**, 245–252, DOI: 10.1016/j.ijhydene.2024.01.194.

8 D. Kaya, I. Demiroglu, I. B. Isik, H. H. Isik, S. K. Çetin, C. Sevik, A. Ekicibil and F. Karadag, Highly Active Bimetallic Pt–Cu Nanoparticles for the Electrocatalysis of Hydrogen Evolution Reactions: Experimental and Theoretical Insight, *Int. J. Hydrogen Energy*, 2023, **48**(95), 37209–37223, DOI: 10.1016/j.ijhydene.2023.06.100.

9 H. Ji, Z. Wu, T. Li, G. Ju, H. Li, Y. Wang, H. Xu and J. Liu, Bipolar Hydrogen Generation via Furfural-Water Co-Electrolysis over Bifunctional CuPt Catalysts, *Int. J. Hydrogen Energy*, 2025, **102**, 856–865, DOI: 10.1016/j.ijhydene.2025.01.096.

10 X. Yang, Z. Lin, X. Cai, A. Cheng, Q. Zhang, Q. Meng, S. Qiu, W. Wang, L. Ma, L. Lin and J. Tan, Shape Control Synthesis of CuPt Alloys with Enhanced Hydrogen Evolution Reaction and Methanol Oxidation Reaction Activities, *ChemNanoMat*, 2021, **7**(11), 1200–1204, DOI: 10.1002/cnma.202100310.

11 J.-W. Zhao, H. Zhang, C.-F. Li, X. Zhou, J.-Q. Wu, F. Zeng, J. Zhang and G.-R. Li, Key Roles of Surface Fe Sites and Sr Vacancies in the Perovskite for an Efficient Oxygen Evolution Reaction *via* Lattice Oxygen Oxidation, *Energy Environ. Sci.*, 2022, **15**(9), 3912–3922, DOI: 10.1039/D2EE00264G.

12 H. Xu, K. Yue, L. Song, H. Zhang, H. Zhu, Z. Zhang and G. Li, The Asymmetrical Fe–O–Se Bonds in $Fe_2O(SeO_3)_2$ Boosting Bifunctional Oxygen Electrocatalytic Performance for Zinc–Air Battery, *Angew. Chem., Int. Ed.*, 2024, **63**(51), e202412025, DOI: 10.1002/anie.202412025.

13 A. P. Tiwari, J. E. Patterson, M. S. Rahman and W. J. Scheideler, Scalable 3D Printed Microlattices of Bimetallic Transition Metal/Metal Oxide Electrocatalysts, *Adv. Mater. Technol.*, 2025, **10**(15), e00122, DOI: 10.1002/admt.202500122.

14 J.-W. Zhao, C.-F. Li, Z.-X. Shi, J.-L. Guan and G.-R. Li, Boosting Lattice Oxygen Oxidation of Perovskite to Efficiently Catalyze Oxygen Evolution Reaction by FeOOH Decoration, *Research*, 2020, **2020**, 6961578, DOI: 10.34133/2020/6961578.

15 C.-F. Li, T.-Y. Shuai, L.-R. Zheng, H.-B. Tang, J.-W. Zhao and G.-R. Li, The Key Role of Carboxylate Ligands in Ru@Ni-MOFs/NF in Promoting Water Dissociation Kinetics for Effective Hydrogen Evolution in Alkaline Media, *Chem. Eng. J.*, 2023, **451**, 138618, DOI: 10.1016/j.cej.2022.138618.

16 S. Anantharaj, S. Noda, V. R. Jothi, S. Yi, M. Driess and P. W. Menezes, Strategies and Perspectives to Catch the Missing Pieces in Energy–Efficient Hydrogen Evolution Reaction in Alkaline Media, *Angew. Chem., Int. Ed.*, 2021, **60**(35), 18981–19006, DOI: 10.1002/anie.202015738.

17 N. C. Minj, B. Kamaraj, S. Mittal, S. Yadav, P. Trivedi and A. Sengeni, Repurposed Cu Scrap Featuring CuO/Cu(OH) 2 Nanostructures as a High-Performance Anode for OER-Masking Small Molecule Electrooxidation, *ACS Sustainable Chem. Eng.*, 2025, **13**(21), 7824–7836, DOI: 10.1021/acssuschemeng.5c00972.

18 S. Anantharaj, H. Sugime and S. Noda, Ultrafast Growth of a Cu(OH)2-CuO Nanoneedle Array on Cu Foil for Methanol Oxidation Electrocatalysis, *ACS Appl. Mater. Interfaces*, 2020, **12**(24), 27327–27338, DOI: 10.1021/acsami.0c08979.

19 S. Anantharaj, H. Sugime, S. Yamaoka and S. Noda, Pushing the Limits of Rapid Anodic Growth of CuO/Cu

(OH) 2 Nanoneedles on Cu for the Methanol Oxidation Reaction: Anodization PH Is the Game Changer, *ACS Appl. Energy Mater.*, 2021, **4**(1), 899–912, DOI: 10.1021/acsaem.0c02822.

20 A. Touni, X. Liu, X. Kang, P. A. Carvalho, S. Diplas, K. G. Both, S. Sotiropoulos and A. Chatzitakis, Galvanic Deposition of Pt Nanoparticles on Black TiO 2 Nanotubes for Hydrogen Evolving Cathodes, *ChemSusChem*, 2021, **14**(22), 4993–5003, DOI: 10.1002/cssc.202101559.

21 K. Huang and R. M. Crooks, Enhanced Electrocatalytic Activity of Cu-Modified, High-Index Single Pt NPs for Formic Acid Oxidation, *Chem. Sci.*, 2022, **13**(42), 12479–12490, DOI: 10.1039/D2SC03433F.

22 P. Wang, Y. Yan, P. Wang, Z. Ye, X. Zheng and W. Cai, Highly Dispersed Pt/CuO Nanoclusters in N-Doped Porous Carbon Array for Superior Hydrogen Evolution, *Chem. Eng. J.*, 2023, **455**, 140856, DOI: 10.1016/j.cej.2022.140856.

23 D. Kaya, I. Demiroglu, I. B. Isik, H. H. Isik, S. K. Çetin, C. Sevik, A. Ekicibil and F. Karadag, Highly Active Bimetallic Pt–Cu Nanoparticles for the Electrocatalysis of Hydrogen Evolution Reactions: Experimental and Theoretical Insight, *Int. J. Hydrogen Energy*, 2023, **48**(95), 37209–37223, DOI: 10.1016/j.ijhydene.2023.06.100.

24 W. Guo, G. Zhu, Y. Zhou, Z. Wang, Z. Pang, Y. Liu, S. Li, B. Zhang, F. Akhtar and P. Feng, Ultra-Low Pt-Decorated Micro/Nanoporous Antennule-like CuOx as Enhanced Trifunctional Electrocatalyst for Water-Splitting and Photocatalytic Degradation of Methyl Orange, *Appl. Surf. Sci.*, 2026, **715**, 164503, DOI: 10.1016/j.apsusc.2025.164503.

25 A. P. Tiwari, M. S. Rahman and W. J. Scheideler, 3D Printed Microlattices of Transition Metal/Metal Oxides for Highly Stable and Efficient Water Splitting, *Adv. Mater. Technol.*, 2024, **9**(13), 2400160, DOI: 10.1002/admt.202400160.

26 J. M. Sieben, A. A. Alvarez and M. D. Sanchez, Carbon-Supported Pt Nanoparticles Modified with CuO for the Electrooxidation of Glycerol in Alkaline Electrolyte, *ACS Appl. Energy Mater.*, 2024, **7**(15), 6677–6686, DOI: 10.1021/acsaem.4c01299.

27 M. Jiang, J. Xu, Q. Zhou, Y. Chen, P. Munroe, L. Li, Z. Xie, Y. Wu and S. Peng, Rationally Designed Asymmetric Pt–O–Cu Ligand to Stabilize Active Sites Towards Superior Industrial–Standard Alkaline Hydrogen Evolution, *Angew. Chem., Int. Ed.*, 2025, **64**(33), e202510259, DOI: 10.1002/anie.202510259.

28 R. Mandavkar, R. Kulkarni, M. Ahasan Habib, S. Burse, S. Lin, S. Kunwar, A. Najar, S. Assa Aravindh, J.-H. Jeong and J. Lee, Super-Porous Pt/CuO/Pt Hybrid Platform for Ultra-Sensitive and Selective H_2O_2 Detection, *Appl. Surf. Sci.*, 2022, **593**, 153454, DOI: 10.1016/j.apsusc.2022.153454.

29 X. Liu, C. Liang, W. Yang, C. Yang, J. Lin and X. Li, A Monodispersed CuPt Alloy: Synthesis and Its Superior Catalytic Performance in the Hydrogen Evolution Reaction over a Full PH Range, *RSC Adv.*, 2021, **11**(21), 12470–12475, DOI: 10.1039/D0RA09386F.

30 F. Sato, T. Naito, S. S. Shah, Z. Cai, G. Chang, Y. He and M. Oyama, Modification of Nickel Wire Electrodes with Platinum in the Presence of Copper Ions via Galvanic Replacement Reactions, *J. Electroanal. Chem.*, 2024, **961**, 118232, DOI: 10.1016/j.jelechem.2024.118232.

31 M. Hamze, M. Rezaei and S. H. Tabaian, Galvanic Replacement of Pt by Cu to Synthesize Highly Active and Durable Pt@Cu/C Anode as Oxygen Evolution Reaction Catalyst, *Colloids Surf., A*, 2023, **656**, 130422, DOI: 10.1016/j.colsurfa.2022.130422.

32 S. R. Anderson, S. Naveen Prasad, E. Della Gaspera, A. P. O'Mullane, V. Bansal and R. Ramanathan, Galvanic Replacement-Driven Fabrication of Photoactive Cu-Pt and Cu-Pd Bimetallic Fabrics for LSPR-Mediated Catalytic Reduction of Ferricyanide, *Mater. Res. Bull.*, 2025, **187**, 113367, DOI: 10.1016/j.materresbull.2025.113367.

33 S. Anantharaj, P. J. J. Sagayaraj, M. S. Yesupatham, R. Arulraj, K. Eswaran, K. Sekar and S. Noda, The Reference Electrode Dilemma in Energy Conversion Electrocatalysis: "Right vs, Okay vs. Wrong", *J. Mater. Chem. A*, 2023, **11**(33), 17699–17709, DOI: 10.1039/d3ta03145d.

34 S. Anantharaj and S. Noda, IR Drop Correction in Electrocatalysis: Everything One Needs to Know!, *J. Mater. Chem. A*, 2022, **10**(17), 9348–9354, DOI: 10.1039/d2ta01393b.

35 S. Anantharaj, S. Noda, M. Driess and P. W. Menezes, The Pitfalls of Using Potentiodynamic Polarization Curves for Tafel Analysis in Electrocatalytic Water Splitting, *ACS Energy Lett.*, 2021, **6**(4), 1607–1611, DOI: 10.1021/acsenergylett.1c00608.

36 S. W. Boettcher, Benchmarks and Protocols for Electrolytic, Photoelectrochemical, and Solar-Thermal Water-Splitting Technologies, *ACS Energy Lett.*, 2020, **5**(1), 70–71, DOI: 10.1021/acsenergylett.9b02441.

37 S. Anantharaj and S. Noda, Dos and Don'ts in Screening Water Splitting Electrocatalysts, *Energy Adv.*, 2022, (8), 511–523, DOI: 10.1039/d2ya00076h.

38 Y. Wang, D. Wang and Y. Li, A Fundamental Comprehension and Recent Progress in Advanced Pt-Based ORR Nanocatalysts, *SmartMat*, 2021, **2**(1), 56–75, DOI: 10.1002/smm2.1023.

39 W. J. Stępniowski, D. Paliwoda, Z. Chen, K. Landskron and W. Z. Misiołek, Hard Anodization of Copper in Potassium Carbonate Aqueous Solution, *Mater. Lett.*, 2019, **252**, 182–185, DOI: 10.1016/j.matlet.2019.05.126.

40 X. Wu, H. Bai, J. Zhang, F. Chen and G. Shi, Copper Hydroxide Nanoneedle and Nanotube Arrays Fabricated by Anodization of Copper, *J. Phys. Chem. B*, 2005, **109**(48), 22836–22842, DOI: 10.1021/jp054350p.

41 D. D. La, S. Y. Park, Y. W. Choi and Y. S. Kim, Wire-like Bundle Arrays of Copper Hydroxide Prepared by the Electrochemical Anodization of Cu Foil, *Bull. Korean Chem. Soc.*, 2010, **31**(8), 2283–2288, DOI: 10.5012/bkcs.2010.31.8.2283.

42 N. K. Allam and C. A. Grimes, Electrochemical Fabrication of Complex Copper Oxide Nanoarchitectures via Copper Anodization in Aqueous and Non-Aqueous Electrolytes, *Mater. Lett.*, 2011, **65**(12), 1949–1955, DOI: 10.1016/j.matlet.2011.03.105.

43 S. M. Pawar, J. Kim, A. I. Inamdar, H. Woo, Y. Jo, B. S. Pawar, S. Cho, H. Kim and H. Im, Multi-Functional Reactively-Sputtered Copper Oxide Electrodes for Supercapacitor and Electro-Catalyst in Direct Methanol Fuel Cell Applications, *Sci. Rep.*, 2016, **6**(1), 21310, DOI: 10.1038/srep21310.

44 S. M. Pawar, B. S. Pawar, A. I. Inamdar, J. Kim, Y. Jo, S. Cho, S. S. Mali, C. K. Hong, J. Kwak, H. Kim and H. Im, *In situ* Synthesis of Cu(OH)2 and CuO Nanowire Electrocatalysts for Methanol Electro-Oxidation, *Mater. Lett.*, 2017, **187**, 60–63, DOI: 10.1016/j.matlet.2016.10.079.

45 S. M. Pawar, B. S. Pawar, B. Hou, J. Kim, A. T. Aqueel Ahmed, H. S. Chavan, Y. Jo, S. Cho, A. I. Inamdar, J. L. Gunjakar, H. Kim, S. Cha and H. Im, Self-Assembled Two-Dimensional Copper Oxide Nanosheet Bundles as an Efficient Oxygen Evolution Reaction (OER) Electrocatalyst for Water Splitting Applications, *J. Mater. Chem. A*, 2017, **5**(25), 12747–12751, DOI: 10.1039/c7ta02835k.

46 H. Xu, J. X. Feng, Y. X. Tong and G. R. Li, Cu2O-Cu Hybrid Foams as High-Performance Electrocatalysts for Oxygen Evolution Reaction in Alkaline Media, *ACS Catal.*, 2017, **7**(2), 986–991, DOI: 10.1021/acscatal.6b02911.

47 Z. Wang, Y. Liu, Y. Cheng, Y. L. Men, P. Liu, L. Zhang, B. Dai and Y. X. Pan, Fast and Efficient Electrocatalytic Oxidation of Glucose Triggered by Cu2O-CuO Nanoparticles Supported on Carbon Nanotubes, *Front. Chem.*, 2022, **10**, 998812, DOI: 10.3389/fchem.2022.998812.

48 H. Zhang, Z. Zhang, N. Li, W. Yan and Z. Zhu, Cu2O@C Core/Shell Nanoparticle as an Electrocatalyst for Oxygen Evolution Reaction, *J. Catal.*, 2017, **352**, 239–245, DOI: 10.1016/j.jcat.2017.05.019.

49 A. Roy, H. S. Jadhav and J. Gil Seo, Cu, 2O/CuO Electrocatalyst for Electrochemical Reduction of Carbon Dioxide to Methanol, *Electroanalysis*, 2021, **33**(3), 705–712, DOI: 10.1002/elan.202060265.

50 J. S. Cho, J. M. Won, J.-H. Lee and Y. C. Kang, Synthesis and Electrochemical Properties of Spherical and Hollow-Structured NiO Aggregates Created by Combining the Kirkendall Effect and Ostwald Ripening, *Nanoscale*, 2015, **7**(46), 19620–19626, DOI: 10.1039/C5NR05930E.

51 L. Geng, Q. Liu, J. Chen, P. Jia, H. Ye, J. Yan, L. Zhang, Y. Tang and J. Huang, In Situ Observation of Electrochemical Ostwald Ripening during Sodium Deposition, *Nano Res.*, 2022, **15**(3), 2650–2654, DOI: 10.1007/s12274-021-3861-6.

52 M. A. Behrens, A. Franzén, S. Carlert, U. Skantze, L. Lindfors and U. Olsson, On the Ostwald Ripening of Crystalline and Amorphous Nanoparticles, *Soft Mater.*, 2025, **21**(12), 2349–2354, DOI: 10.1039/D4SM01544D.

